Available online at www.sciencedirect.com
ScienceDirect
Acta Materialia 57 (2009) 570–581
Acta MATERIALIA
www.elsevier.com/locate/actamat

Evaluation of crack-tip stress fields on microstructural-scale fracture in Al–Al_2O_3 interpenetrating network composites

Robert J. Moon [a], Mark Hoffman [a,*], Jürgen Rödel [b], Shigemi Tochino [c], Giuseppe Pezzotti [c]

[a] School of Materials Science and Engineering, The University of New South Wales, NSW 2052, Australia
[b] Institute of Materials Science, University of Technology-Darmstadt, Darmstadt D-64287, Germany
[c] Department of Materials, Ceramic Physics Laboratory, Kyoto Institute of Technology, Sakyo-ku, Matsugasaki, 606-8585 Kyoto, Japan

Received 28 August 2008; received in revised form 26 September 2008; accepted 27 September 2008
Available online 7 November 2008

Abstract

The influence of local microstructure on the fracture process at the crack tip in a ceramic–metal composite was assessed by comparing the measured stress at a microstructural level and analogous finite element modelling (FEM). Fluorescence microprobe spectroscopy was used to investigate the influence of near-crack-tip stress fields on the resulting crack propagation at the microstructural scale. The high spatial resolution was effective at mapping the localized crack-tip stress distributions within the complex Al–Al_2O_3 phase morphologies, where the localized stress distribution about the crack tip within the Al_2O_3 phase could be measured. Regions of high-localized tensile stress within the microstructure resulting from a combination of applied load and thermal residual stress were identified and could be used in predicting the subsequent crack extension direction. Stress distributions calculated from spectroscopy results were compared with microstructural level FEM of the same structure and general agreement between the two techniques was observed.
© 2008 Acta Materialia Inc. Published by Elsevier Ltd. All rights reserved.

Keywords: Ceramic matrix composites; Fracture; Residual stresses; Finite element analysis; Raman spectroscopy

1. Introduction

Composite materials are designed to optimize material performance. By varying the component materials and the reinforcement phase geometry (e.g. particle/matrix, fibre/matrix, co-continuous, laminar or graded structure), the resulting mechanical and fracture behaviours can be modified. The fracture behaviour of a material is dependent on the strain energy release rate, G, the intrinsic work of fracture (fracture resistance), R, and the stress distribution acting at the crack tip. A crack will propagate along a path, for a given crack-tip loading condition (tensile and shear), which maximizes the difference between G and R. In single-phase homogeneous materials, R and G are effectively constant and, for a given crack-tip loading condition, crack paths can be predicted by maximizing G. However, in multiphase composites the fracture behaviour on a microstructural scale is difficult to predict because G, R and the crack-tip loading condition all vary due to differences between the phases (e.g. stiffness, strain to failure, plasticity, interfacial energy, the variation in residual thermal stress and microcracking). As a consequence, complex crack propagation paths and crack bridging result, contributing to increased fracture resistance. The interaction of physical property differences between the phases and the resulting stress distributions amongst the phases give composites their superior fracture strengths. However, it also presents particular challenges in predicting their performance.

Experimental verification of crack-tip stress distributions within composite microstructure is necessary for the development of models that can simulate fracture events within composites. The crack-tip strain and resulting stress distributions within composites have been an active field of theoretical [1–5] and experimental [6–16] research, where the influence of composite structure, thermal stresses and reinforcement phase geometry, shape, size, stiffness, location, distribution and interfacial strength have been inves-

* Corresponding author.
E-mail address: mark.hoffman@unsw.edu.au (M. Hoffman).

1359-6454/$34.00 © 2008 Acta Materialia Inc. Published by Elsevier Ltd. All rights reserved.
doi:10.1016/j.actamat.2008.09.043

tigated. However, the majority of the crack-tip stress investigations involve analytical and numerical modelling with no or limited experimental verification, or the experimental techniques do not have sufficient resolution to measure the reinforcement–crack-tip interactions.

Experimental verification of strain distributions within each phase of a composite is non-trivial and requires measurement techniques that combine high strain resolution with high spatial resolution. Additionally, the strain within the bulk is different to that at the surface, due to mechanical constraint, thus a distinction must be made regarding the measured region. Since the majority of the crack tip is located within the bulk rather than at the surface, the bulk crack-tip strain distribution may be more indicative of predicting the fracture behaviour. However, the bulk strain measurements are averaged through the sample thickness making it difficult to associate a measured strain to a particular location or feature within the composite structure. The strain distribution within the bulk has been measured by neutron diffraction [17,18] and high-energy X-ray diffraction [13,14] techniques. Hanan et al. [13] and Preuss et al. [14] used high-energy X-rays to evaluate the strain distribution in Ti–SiC fibre composites with artificially introduced flaws and cracks. The introduction of the flaw/crack within the composite was shown to alter the resulting strain in the matrix and in the fibre phase, however, there was insufficient spatial resolution to investigate how the reinforcement phase modified the localized crack-tip stress field.

Experimental studies investigating crack-tip strain fields have typically used techniques that measure strain at the sample surface. Macroscopic strain fields, at a size scale greater than that of the reinforcement phase, have been measured by optical interferometry [9], low energy X-ray diffraction, thermo-elasticity [15] and the caustic method [10]. These techniques have been used, with some success, to relate the long-range crack-tip strain distribution to the resulting crack-tip stress intensity factor and fracture behaviour. However, the low spatial resolution limits the ability to investigate the influence of the reinforcement phase on the localized stress distribution near the crack tip.

Raman and fluorescence spectroscopy techniques ($\sim$1 μm spot size) have been used on composites to measure the microscopic strain fields, which are smaller than the size of the reinforcement phase, to quantify crack-bridging tractions [7,19,20] and stress distributions in the neighbourhood of crack tips [7,11,12,16]. Bennett and Young [7] investigated the fibre–crack interaction in an aramid/epoxy fibre–matrix composite by measuring the strain distribution along the fibre axis for a fibre positioned at the crack tip. A single line measurement was taken along the fibre length, and it was observed that there was maximum strain within the fibre in the immediate vicinity of the crack tip, which decreased exponentially with increasing distance from the crack tip. The studies by Miyagawa et al. [11,12] measured the exponential reduction in strain distribution within the matrix phase of carbon fibre reinforced plastic as a function of distance from the crack tip, but the matrix–reinforcement phase interaction was not investigated. These works demonstrated the usefulness of Raman spectroscopy for the measurement of strain in the neighbourhood of the crack tip. However, since only single line scans were used, the interaction of the reinforcement–matrix and reinforcement–crack-tip interactions were not completely observed, limiting the amount of information gain from the studies. Highlighting this, Moon et al. [16] mapped the crack-tip stress distribution within Al–Al_2O_3 composites having complex phase morphology, and found a large asymmetrical stress distribution surrounding the crack tip.

The Raman and fluorescence spectroscopy techniques measure the transition energy between electronic or vibrational states that is characteristic of the atomic bonding within the material and results in a material-specific spectrum. Stress within a material can be measured based on the piezospectroscopic effect, where an applied load strains the material lattice, altering the transition energy between vibrational states which shifts the measured material spectrum [20–23]. For alumina, the R1 and R2 fluorescence lines of Cr^{3+} substitutional impurities are measured because of their sharp, high-intensity spectra that are typically centred at reduced wave numbers of $\sim$14,400 cm^{-1} and $\sim$14,440 cm^{-1}, respectively [23,24]. However, the spectra will shift as a result of applied stress, residual stress, sample temperature and impurity content [21–24].

Previous studies on Al–Al_2O_3 composites with interpenetrating network phase structures have investigated the stress distributions [16–18,23,25–27] and fracture behaviour [25,28–31]. Three types of stress distributions have been investigated: thermal stress distribution [16–18,23,25,27], crack-bridging [20,27,30,31] and crack tip [16]. Theoretical [23,26] and experimental [16–18,25,27] studies have found that the thermal stress within each phase is not constant but varies in magnitude and location within the structure. The composite fracture behaviour has been described in terms of fracture toughness, and crack growth resistance behaviour (*R*-curve). However, the influence of microstress distribution and its influence on fracture behaviour at the microstructural scale has not been investigated.

The purpose of the present study was to use fluorescence spectroscopy combined with finite element modelling (FEM) to map the residual thermal stress and the crack-tip stress fields that develop in Al–Al_2O_3 composites, and relate the observed stress distribution to the resulting fracture behaviour at the microstructural scale.

2. Experimental procedures

2.1. Sample preparation

Interpenetrating Al–Al_2O_3 composites were produced by liquid metal infiltration into ceramic performs using the infiltration technique in Refs. [28,32] and is described

briefly here. The ceramic preforms were produced via colloidal infiltration of open-celled polyurethane foams (Bulpren S-31048, Eurofoam, Troisdorf, Germany). Initially, the foam had a relative density of 2.5% and a pore size of ~0.28 mm (corresponding to 90 pores per inch from the manufacture), which was compression moulded to the desired relative density [33]. The foam was then infiltrated with an alumina slip (25 vol.% solids, 99.99% Al_2O_3, <1 ppm Cr, Taimicron TM-DAR, Taimei Chemicals Co., Ltd.) and dried. The resulting piece was fired in a two-step process to pyrolize the foam (by heating to 400 °C at 0.5 K min^{-1} and to 800 °C at 0.7 K min^{-1}) and then sinter the ceramic (1500 °C for 60 min in air). The porous alumina preforms were then infiltrated with aluminium using a pressure infiltration process (1050 °C under 10 MPa argon gas for 2 h) outlined in Refs. [28,32]. The final product was >99% of theoretical density. The morphology of its aluminium and polycrystalline alumina regions resulted from the compressed structures of the foam ligaments and pores, respectively.

Two composites were produced: 3 vol.% Al–97 vol.% Al_2O_3 (3Al) and 30 vol.% Al–70 vol.% Al_2O_3 (30Al). Tiles were surface-ground flat using a 600 grit diamond wheel and multiple bend bars measuring 4 mm × 3 mm × 40 mm were then cut from the tile. The 4 mm × 40 mm side surfaces were additionally polished to 1 μm diamond abrasives. Single-edge V-notched beams (SEVNB) were produced by cutting a straight V-notch of length 1.5 mm across the 3 mm × 40 mm face, perpendicular to the length of the bend bar [34], producing a final notch-tip diameter of ~25 μm. A crack was initiated from the V-notch tip by loading the sample in a three-point bending load fixture (16 mm span width) in a screw-driven mechanical testing machine with a displacement rate of ~0.05 mm min^{-1}. The 3Al composite had a crack initiation toughness of $K_i = 4.3$ MPa $m^{1/2}$, which produced a 673 μm crack from the notch tip. In comparison, the 30Al composite had a crack initiation toughness of $K_i = 6.2$ MPa $m^{1/2}$, producing a 420 μm crack from the notch tip. Thus, for subsequent crack-tip stress measurements both samples were under large scale bridging conditions [35].

One additional composite, 3 vol.% epoxy–97 vol.% Al_2O_3 (3epoxy), was produced following the method described above, with the porous ceramic preform being infiltrated with epoxy (Epofix, Struers, Germany) [36]. This composite was used to assess the thermal stress distribution within the alumina phase that resulted from thermal expansion anisotropy of the alumina phase.

2.2. Fluorescence spectroscopy

Fluorescence spectroscopy was used to measure the stress distribution within the alumina phase by the piezospectroscopic assessment of the R1 and R2 fluorescence lines. The sample surface was irradiated with an Ar^+ ion laser (wavelength of 488 nm, at 200 mW power) in which a confocal optical microscope was used to both focus the laser on the sample surface and collect its scattered radiation. The laser beam was focused on the sample surface, but, due to the translucency of polycrystalline alumina, the interaction volume of the laser light encompassed a region from the surface to several tens of microns below the surface (~30 μm for polycrystalline 100 vol.% alumina), so the resulting measured frequency was a Gaussian average over this volume [20]. It was assumed that the interaction volume of the laser light was constant for every point measured in the composite material and that the stress field is three-dimensional (3D). A triple monochromator (NR T64000, Jobin-Yvon/Horiba, Tokyo, Japan) equipped with a CCD detector was used to perform the analysis. A neon discharge lamp was used as a frequency calibration standard.

The pre-cracked bend bars were loaded in a three-point bend fixture (16 mm span width and equipped with a 100 N load cell) positioned on the microscope stage of the Raman spectroscopic apparatus. An automatic traveling stage, having a 1 μm lateral displacement resolution, was used to direct the laser spot to the desired locations on the sample surface, allowing for fluorescence spectra maps to be made. Both low- and high-resolution maps of the region surrounding the crack tip were measured, in which individual fluorescence spectra, each of 1 s acquisition time, were collected over the desired areas. Low-resolution maps measured an area of ~1000 μm × ~1200 μm using a laser spot size of 10 μm, and spectra were obtained over a 10 μm grid-like array of points within this selected area. For the high-resolution maps, an area of ~250 μm × ~250 μm was measured using a laser spot size of 5 μm, and the spectra were obtained over a 5 μm grid-like array of points within this selected area. All experiments were conducted in an isolated environmentally controlled room at 24 ± 1 °C.

The fluorescence spectra were analysed with curve-fitting algorithms included in the LabSpec software package (Horiba Co., Kyoto, Japan) to estimate the R1 peak intensities and peak wave numbers. Note that the neon standard spectra directly overlapped with the alumina R2 fluorescence peak; consequently the R2 peak was not used in the analysis. The trace of the principal stress tensor (henceforth, simply referred to as "hydrostatic stress"), $\langle\sigma\rangle$, was calculated by the shift in wavelength, $\Delta\nu$, of the R1 alumina fluorescence spectra line, obtained from the difference between the peak centres of the stressed and unstressed conditions, via the relation

$$\langle\sigma\rangle = \frac{\Delta\nu}{\langle\Pi\rangle} \tag{1}$$

where $\langle\Pi\rangle$ is the 3D R1 piezospectroscopic coefficient, defined as $\langle\Pi\rangle_{3d} = \Pi_{11} + \Pi_{22} + \Pi_{33}$, with $\Pi_{11} = 2.56$ cm^{-1} GPa^{-1}, $\Pi_{22} = 3.5$ cm^{-1} GPa^{-1} and $\Pi_{33} = 1.53$ cm^{-1} GPa^{-1} [22]. A detailed description of the foundations of the stress analysis technique is given in Ref. [20]. Note that the R1 line frequency shifts along the *a*-axis in single-crystal sapphire have been reported to be slightly non-linear [22]; however, for polycrystalline alu-

mina subjected to small changes in stress (~500 MPa), the deviations from linearity are within the scatter of the data [21,23].

The unstressed alumina R1 absolute wave number used in the stress calculations was estimated using the 3epoxy composite, and was obtained from averaging 2600 individual spectra taken over a ~250 μm square area, using a 5 μm laser spot size and a 5 μm grid-like array of points within this selected area. Minimal residual thermal stresses would be imparted onto the alumina by the epoxy due to the low epoxy modulus, its low volume fraction and its room temperature curing. Additionally, the stress distribution within the alumina phase, resulting from thermal expansion anisotropy of the alumina phase, will be averaged out due to the large number of spectra taken and because the fluorescence interaction volume was many times larger than the average alumina grain size (~1 μm). This averaging is partially supported by the small standard deviation of the measured R1 absolute wave number of 0.013 (cm^{-1}). Note that the stress distributions in alumina due to its thermal expansion anisotropy would be much lower than the stress distributions developed from the thermal expansion mismatch within the Al–Al_2O_3 composites [17].

For the 3Al and 30Al composites, since the R1 fluorescence spectrum is specific for alumina, and aluminium does not fluoresce within this wave number range, the aluminium regions have spectra intensities equivalent to the background noise. The regions within the map area having R1 intensities below 10% of the maximum intensity were considered to have an increased likelihood of having the R1 wavelength influenced by the background noise of the system. These regions were therefore not considered, and were coloured white in the resulting stress maps.

2.3. Crack-tip stress measurement

The crack-tip stress distributions are influenced by the applied load, residual stress and crack-bridging, and the resulting crack-tip stress intensity factor is the sum of these contributions, K_a, K_r and K_b, respectively

$$K_{tip} = K_a + K_r + K_b \quad (2)$$

In general, K_{tip} decreases with lower applied loads, compressive thermal residual stress and crack-bridging, which applies closure stresses along the crack length. The general effect of crack bridging is to shield the crack tip from stresses that would otherwise develop from a given applied load. The composites tested in this study will have a K_{tip} lower than K_a because crack bridging by the ductile phase shields the crack tip from stress.

Fluorescence spectroscopy was used to measure the hydrostatic stress contribution of applied load, residual stress and crack bridging on crack-tip stress distribution. To do this, three separate stress distributions were calculated: thermal stress distributions ($K_a = K_b = 0$), total crack-tip stress distribution ($K_a + K_r + K_b$) and the crack-tip stress distribution resulting from an applied mechanical load ($K_r = 0$, $K_b \neq 0$). The thermal stress distribution, resulting from sample processing and influenced by the presence of a crack, was calculated from the spectra measurements with near-zero applied load on the bend bar that resulted in a small applied stress intensity factor, $K_a = \sim 0.1$ MPa $m^{1/2}$. With a small applied load, contributions to the crack-tip stress from the applied load and crack bridging would be minimal.

For the crack-tip stress distributions the applied load was chosen to maximize the crack-tip stress without causing subsequent crack extension. The idealized criteria of $K_a \approx 90\%$ K_i, was used, in which the actual values used were $K_a = \sim 4.1$ MPa $m^{1/2}$ for 3Al composite and $K_a = \sim 5.5$ MPa $m^{1/2}$ for the 30Al sample. The total crack-tip stress distribution was calculated from the spectra measurements with an applied load, residual thermal stress and crack-bridging stress. The calculation of the crack-tip stress distribution resulting from the applied load is more involved. The R1 spectra maps measured from the mechanically loaded sample have components from the pre-existing residual thermal stress, the external applied load and crack bridging. To remove the influence of the residual stress, the spectra maps from the unloaded samples were subtracted from those of the loaded samples. The resulting shifts in the final R1 spectra represent the stresses that developed from the external applied load. For the composites tested in this study, $K_b < 0$, thus crack bridging will lower the crack-tip stress due to the externally applied load alone.

2.4. Crack growth resistance measurement

After the stress measurements were completed, the pre-existing crack was further extended. Controlled short crack extensions, ~35 μm incremental growth, were accomplished by in situ measurements using a four-point bend fixture (10 mm inner and 20 mm outer loading spans), combined with a specialized applied loading technique to promote subcritical crack growth [29,37,38]. The fracture path was observed and the crack growth resistance was measured for both 3Al and 30Al composites.

3. Finite element modelling

For the 3Al composite, the FEM measurements of the hydrostatic crack-tip stress distributions were compared with the results from the fluorescence spectroscopy. For simplicity, comparison between the FEM and fluorescence spectroscopy measurements were completed with the same applied crack-tip stress of $K_a = \sim 4.1$ MPa $m^{1/2}$. Additionally, since the crack-tip stress fields are also influenced by thermal residual stress and crack bridging, these components were included in the FEM. By doing so, the K_{tip} will be approximately the same between FEM and the experimentally measured crack-tip stress, allowing for a more representative comparison. FEM was not undertaken for the 30Al composite because of the complexity of the microstructure and the crack-microstructure interaction.

FEM simulations were completed using ANSYS (Version 8.0, ANSYS Inc., Canonsburg, PA). The specimen geometry and the experimental three-point bend fracture test of the pre-cracked 3Al bend bar were duplicated (Fig. 1). In the neighbourhood of the crack tip, the geometry of the actual composite microstructure was duplicated, allowing for a direct comparison between the experimental stress measurements and the simulated ones. This simulated microstructure was then embedded in a homogeneous effective medium of the composite for applying suitable boundary constraints. Free meshing was used with mesh refinement around the crack tip and reinforcement–matrix phase interfaces, as shown in Fig. 2.

The composite structures were modelled in two-dimensions under plane stress conditions using the two-dimensional (2D) eight-node structural solid elements. The crack-tip singularity was modelled using triangular singular elements. The alumina was considered to behave fully elastically, while the aluminium was considered to behave in an elastic/plastic manner. The aluminium non-linear deformation behaviour was simulated using the von Mises yield criterion coupled with an isotropic work hardening, in which the stress–strain behaviour measured by Kocks [39] was used. Thermal stresses were considered to develop on cooling from 400 °C to room temperature, as determined by Hoffman et al. [17], who measured thermal residual strains and stresses in similar Al–Al_2O_3 interpenetrating composites. Thermal stress was addressed by considering the resulting body force at each node from a uniform temperature change across all nodes from 400 to 25 °C. It was assumed that no debonding occurred at the aluminium–

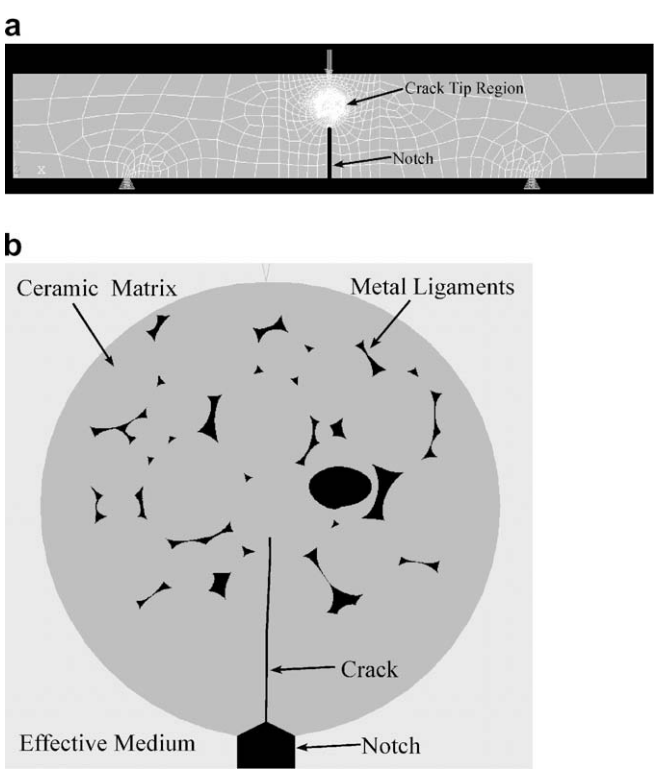

Fig. 1. FEM geometry. (a) Three-point bending of a pre-cracked notched bend bar, in which finer meshing was used near the crack-tip region. (b) 3Al composite where, in the neighbourhood of the crack tip, the Al–Al_2O_3 microstructure was duplicated and surrounded by an effective medium.

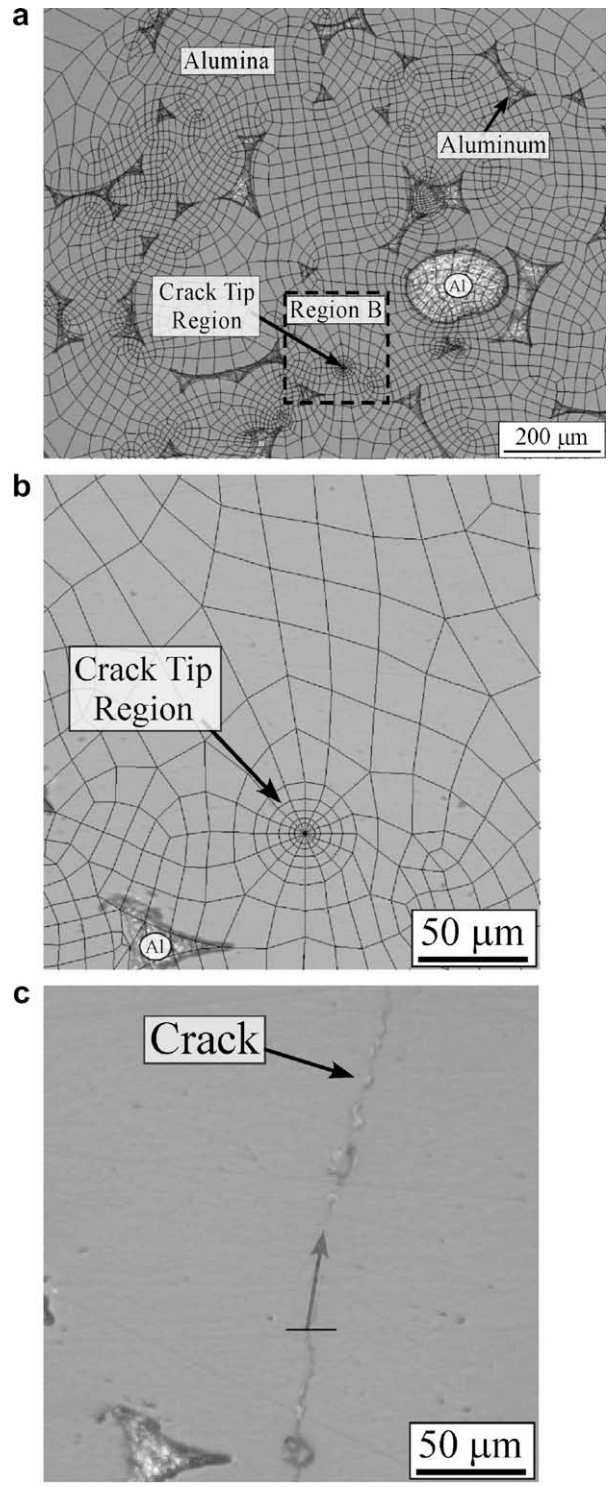

Fig. 2. Optical micrographs of the 3Al composite with FEM mesh overlaid for the two mapping areas: (a) low-resolution Raman measurements and (b) high-resolution Raman measurements (region B). (c) The resulting crack profile after further crack extension, in which a crack deflection angle was $\theta \sim 8°$. The horizontal line marks the initial crack-tip location.

alumina interfaces. The material properties are summarized in Table 1.

The contribution of crack bridging by the ductile aluminium phase on FEM crack-tip stress was accounted for by applying crack closure tractions along the crack surfaces via surface pressures which varied as a function of distance behind the crack-tip according to [40,41]

$$\sigma_{\mathrm{br}}(x) = \sigma_{\max}\left(1 - \left(\frac{x}{L}\right)^{\frac{1}{2}}\right)^{n} \tag{3}$$

where $\sigma_{\max}$ is the maximum stress supported by the bridging zone, n is a softening coefficient, x is the distance from the crack tip and L is the steady-state bridging zone length, i.e. the critical distance behind the crack-tip where closure stresses exist. The measured 3Al crack growth resistance (R-curve) was used to determine these constants. Initially, a weight function analysis described by Moon et al. [40,41] was used to produce a predicted R-curve, in which Eq. (3) was used to apply the necessary crack closure tractions. The predicted R-curve was fitted to the experimentally measured R-curve by adjusting the constants until there was direct overlap. The resulting constants were found to be: $\sigma_{\max} = 30$ MPa, $n = 1$ and $L = 900$ μm.

The FEM simulations focused on the stress distributions around the pre-existing crack-tip resulting from thermal stresses, the load applied to the bend bar and the combination of these two. The crack-tip stress intensity factors, k_{I} and k_{II} (modes I and II, respectively), were calculated from the displacements of nodes on the crack flanks close to the crack tip.

4. Results

4.1. Microstructure

The microstructures of the 3Al and the 30Al materials are shown in Figs. 2 and 3, respectively. Parts a and b show the location of the crack in relation to the surrounding microstructure, and the exact location of both the low- and high-resolution stress maps given in Figs. 4–7. The foam compaction significantly altered the sacrificial structure used as a template for composite processing and resulted in different phase morphologies within the 3Al and 30Al composites. This difference in microstructure between 3Al and 30Al implies that there should be differences in the measured crack-tip stress distributions and in the observed fracture behaviour.

Table 1
Material properties.

Material	Elastic modulus (GPa)	Poisson's ratio, ν	Coefficient of thermal expansion, α (10^{-6}/°C)
Al	70.7 [45]	0.34 [45]	23.2[a]
Al_2O_3	390 [49]	0.25 [46]	5.7[b]
3Al (3 vol.% Al–97 vol.% Al_2O_3)	362 [52]	0.3	8[c]

[a] Averaging of the results from the following Refs. [46–48].
[b] Averaging of the results from the following Refs. [46–48,50,51].
[c] Estimated from the effective medium approximation.

4.2. Fracture behaviour

Crack propagation within the composite occurred preferentially within the alumina phase (Figs. 2c and 3). This was expected because the alumina has a lower failure strain, lower fracture energy and a higher modulus, which brings about higher stresses from the applied load. For the 3Al composite, crack paths were relatively straight, with smooth changes in the crack direction as the crack moves to avoid intersecting the metal reinforcement phase. Nonetheless, the interpenetrating phase structure ensures that crack-bridging occurs within the bulk. The crack opening directly behind the crack tip was extremely small, making it difficult to discern the crack in Fig. 2. An accurate crack-tip location was obtained in which the FEM mesh in Fig. 2b shows the location of the crack tip within 5 μm. Crack initiation toughness for 3Al was $K_{\mathrm{i}} = 4.3$ MPa m$^{1/2}$, and the initial crack propagated to a length of 673 μm. For subsequent crack extension the effective toughness was $K_{\mathrm{R}} = 5.5$ MPa m$^{1/2}$, which slowly increased with further crack extension to $K_{\mathrm{R}} = 8.4$ MPa m$^{1/2}$ at a final crack length of 1190 μm, demonstrating that this material experiences crack growth resistance. The fracture and R-curve results are consistent with previous experimental work [27,28,30].

For the 30Al composite, there was discontinuous crack growth and crack kinking (Fig. 3). The crack extended through an alumina region but, once it impinged on an aluminium–alumina interface, it was observed to reinitiate either in the same alumina region or in a subsequent alumina area, resulting in ~50 μm lateral displacement of the crack extension path. As the crack extended through subsequent alumina regions it was then bridged by the metallic reinforcement phase. Typically, the crack-tip ended at an aluminium–alumina interface. The crack opening directly behind the crack-tip region was much larger than for the 3Al sample, allowing for the crack to be easily observed in Fig. 3. Crack initiation toughness for 30Al was $K_{\mathrm{i}} = 6.2$ MPa m$^{1/2}$, resulting in a crack length of 420 μm. For subsequent crack extension the effective toughness was $K_{\mathrm{R}} = 7.0$ MPa m$^{1/2}$, which increased with further crack extension to $K_{\mathrm{R}} = 10.1$ MPa m$^{1/2}$ at a final crack length of 770 μm. The fracture and R-curve results are consistent with previous experimental work [27,28,30].

4.3. Crack-tip stress fields

The measured and FEM-predicted stress fields for the 3Al composite are shown in Figs. 4 and 5, in which the stress contours are labelled with ovals (measured stress) and rectangles (FEM predicted). The measured stress fields for the 30Al composite are given in Figs. 6 and 7, in which the stress contours were difficult to show due to the large stress distribution and the discontinuous phase microstruc-

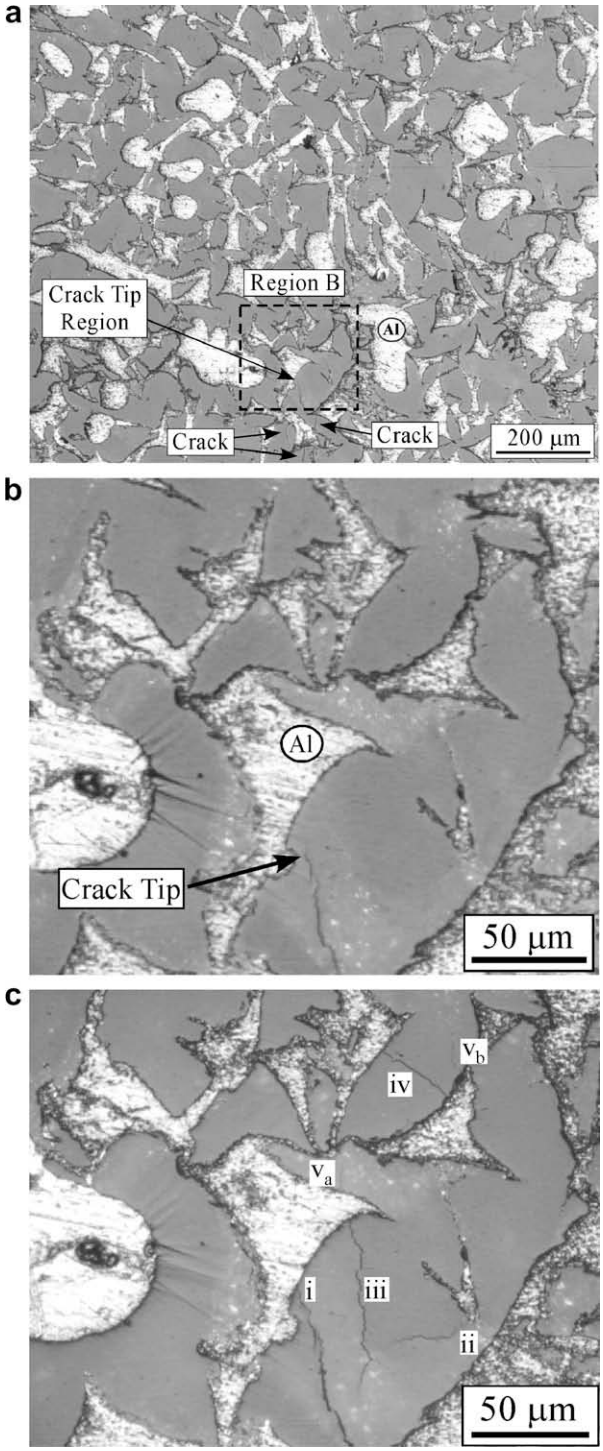

Fig. 3. Optical micrographs of the 30Al composite for the two mapping areas: (a) low-resolution Raman measurements and (b) high-resolution Raman measurements (region B). The resulting crack profile after further crack extension is given in (c).

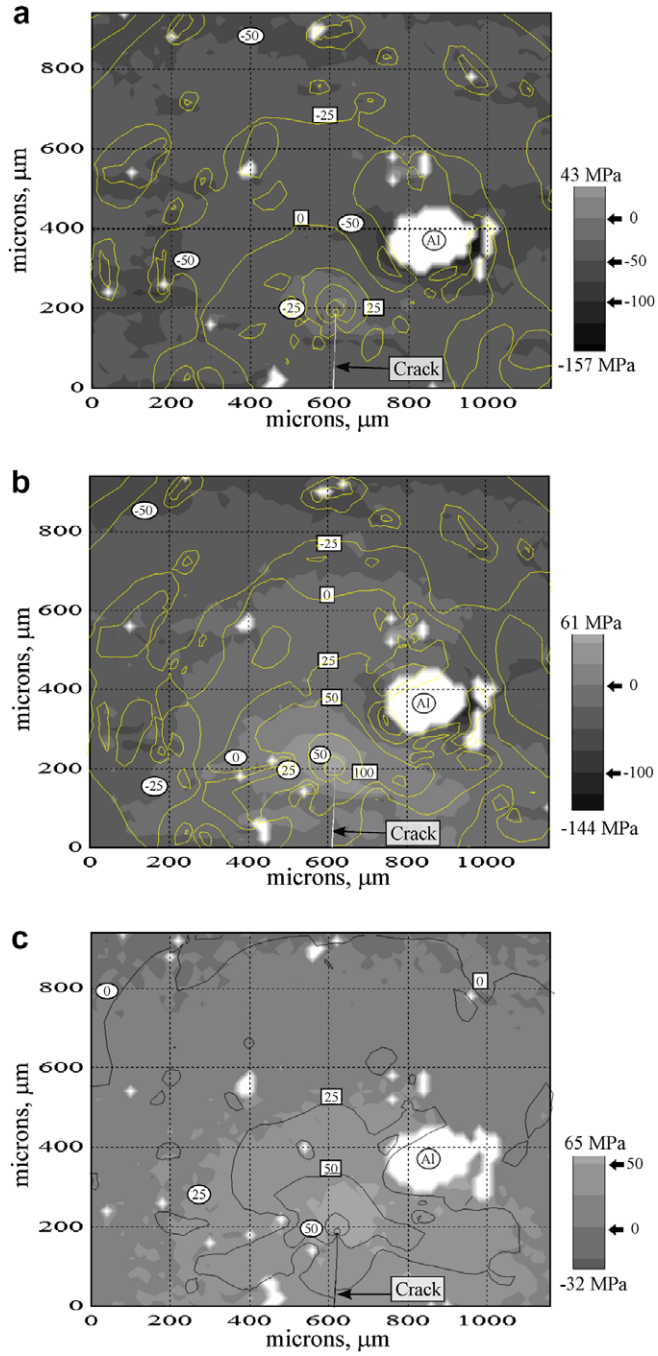

Fig. 4. The measured and FEM-simulated hydrostatic stress maps for 3Al, low-resolution. (a) Thermal stress distribution, (b) total stress distribution and (c) applied load crack-tip stress distribution. The measured stress contours are marked via oval labels and the legend, while FEM contours are marked with rectangular labels. All stresses are in MPa and the FEM contours are: −25, 0, 25, 50, 100 and 200 MPa.

ture. For all stress maps the regions coloured in white were areas where the stress was not calculated due to the low spectra intensity; these generally corresponded to the aluminium areas. The alignment of the microstructure in Figs. 2 and 3 with the corresponding stress maps (Figs. 4–7) is observed by noting that the most prominent aluminium feature is marked with the label "Al". For the low-resolution maps (Fig. 4 and 6), it was observed that not all the aluminium areas were coloured white, as would be expected. This resulted from the limited spatial resolution caused by the combined effects of the ~10 μm laser spot size and by the ~10 μm step size of the mapping sequence. In contrast, for the higher-resolution maps (Figs. 5 and 7), much finer features in the microstructure could be detected,

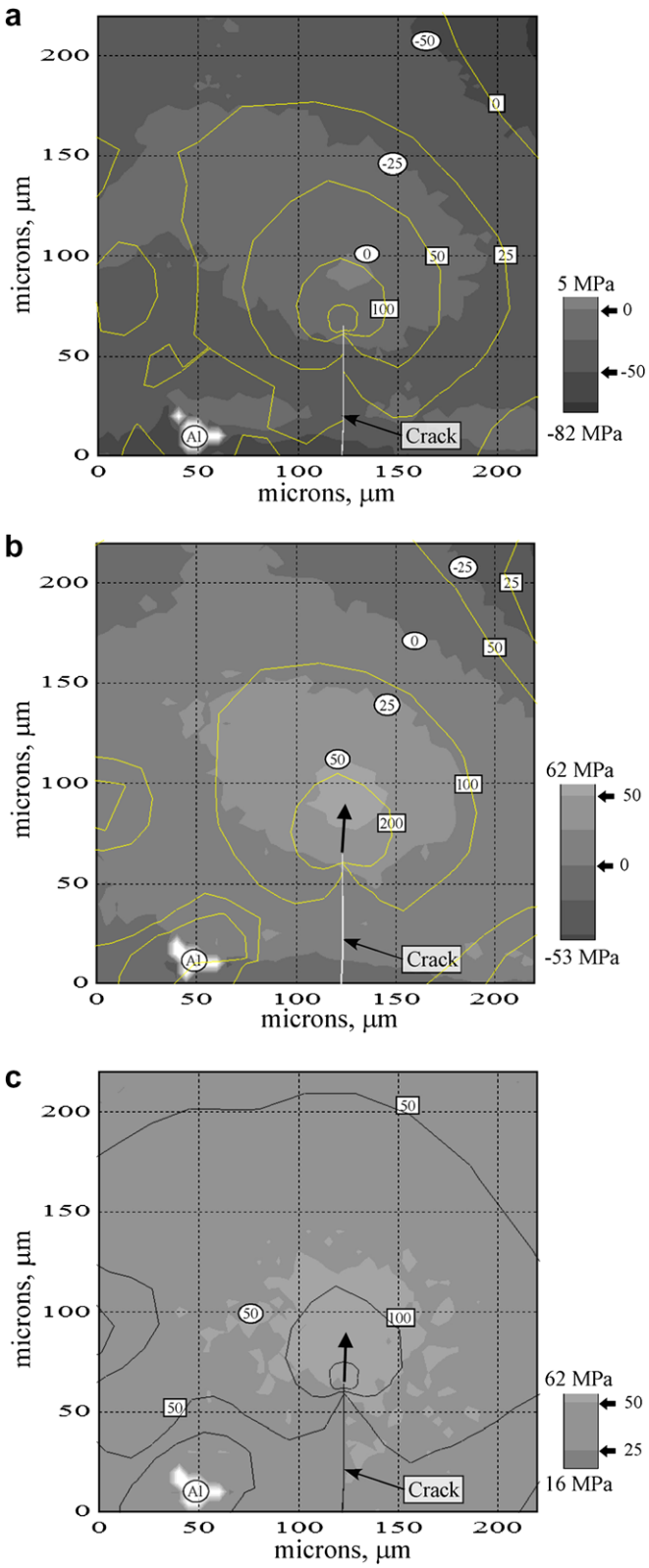

Fig. 5. The measured and FEM-simulated hydrostatic stress maps for 3Al, high-resolution. (a) Thermal stress distribution, (b) total stress distribution (the arrow marks the predicted crack deflection angle of $\theta \sim 3.5°$) and (c) applied load crack-tip stress distribution (the arrow marks the predicted crack deflection angle of $\theta \sim 1°$). The measured stress contours are marked with oval labels and the legend, while FEM contours are marked with rectangular labels. All stresses are in MPa and the FEM contours are: −25, 0, 25, 50, 100 and 200 MPa.

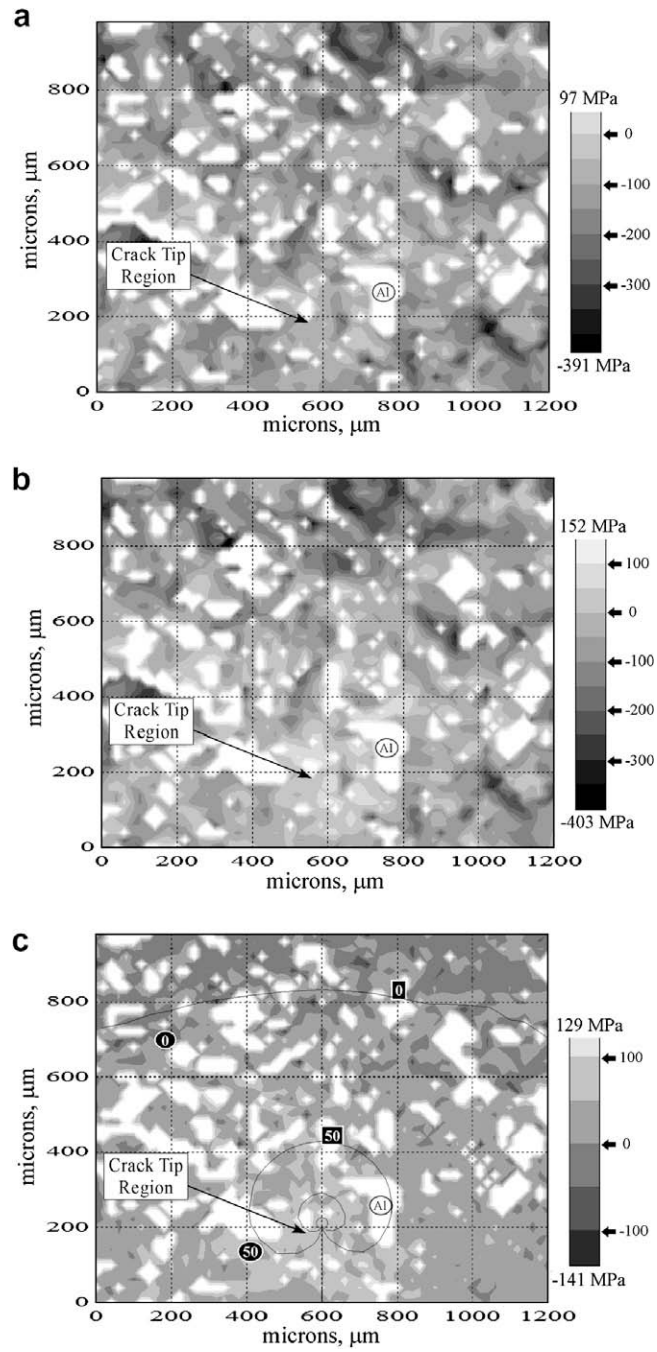

Fig. 6. The measured hydrostatic stress maps for 30Al, low-resolution. (a) Thermal stress distribution, (b) total stress distribution and (c) applied load crack-tip stress distribution, showing a nearly symmetrical stress distribution about the crack-tip region. The measured stress contours are marked with oval labels and the legend, while FEM contours are marked with rectangular labels. All stresses are in MPa and the FEM contours are: 0, 50, 100 and 200 MPa.

and nearly all of the aluminium regions were coloured white. The stress distributions around feature sizes of ~20 μm could be resolved.

For the 3Al composite the thermal, total and applied load crack-tip stress distributions for the low- and high-resolution maps are given in Figs. 4 and 5, respectively. With the crack-tip located in the centre of the alumina region,

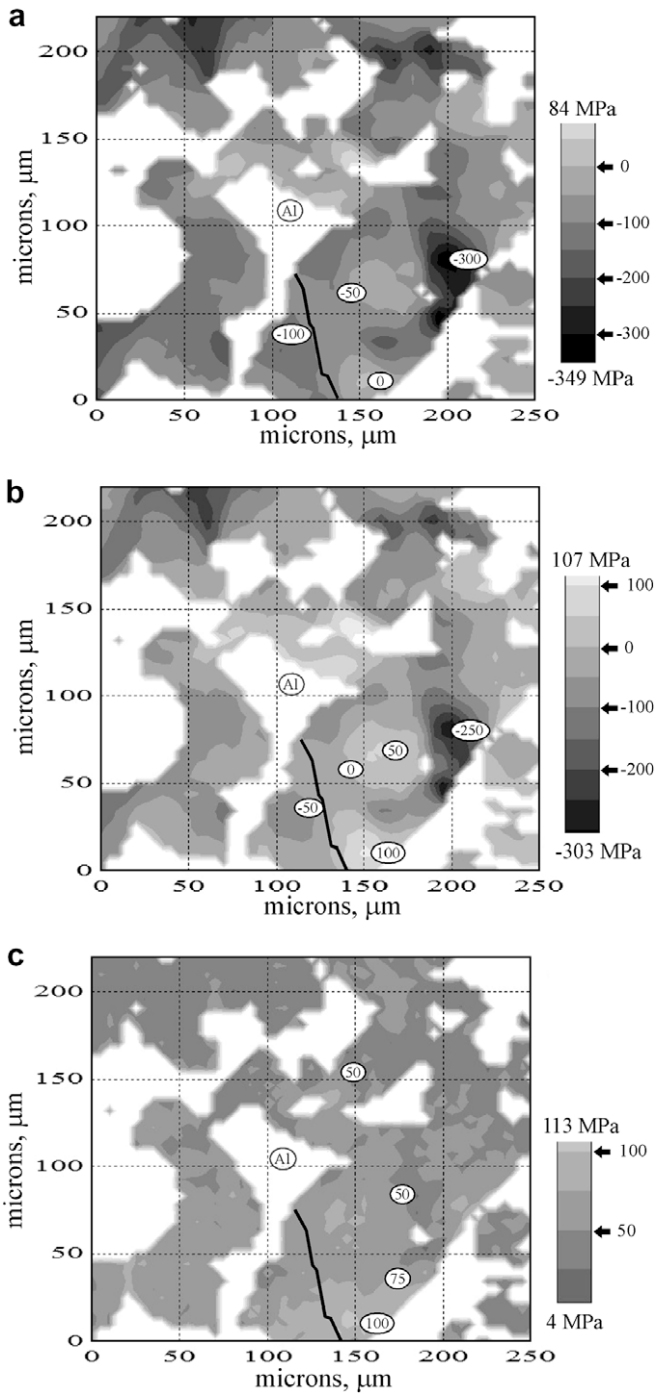

Fig. 7. The measured hydrostatic stress maps for 30Al, high-resolution. (a) Thermal stress distribution, (b) total stress distribution and (c) applied load crack-tip stress distribution, showing that there is no stress concentration at the crack tip. The measured stress contours are marked with oval labels and the legend, while FEM contours are marked with rectangular labels. The thick black line shows the location of the crack. All stresses are in MPa.

the localized crack-tip stresses could be measured. The thermal stress distributions from 43 to −157 MPa in the low-resolution map and from 5 to −82 MPa in the higher-resolution map demonstrate the variable stress within the alumina phase. The difference in stress range is due to the larger sampling area of the low-resolution map, which included the area around the large alumina inclusion labeled "Al". The effect of the applied load was to increase the stress concentration at the crack tip. By removing the influence of the thermal stress, the crack-tip stress field resulting solely from the applied load is more clearly differentiated (Figs. 4c and 5c).

The measured stress contours for the low- and high-resolution maps are reasonably consistent with each other in terms of the magnitude, shape and spacing of the given contours from the crack tip, and give an indication as to the correlation of the measurement technique to predicted behaviour. The asymmetric nature of the crack-tip stress contours demonstrates that the presence of the aluminium phase within the alumina matrix modifies the stress distributions. In contrast, homogeneous materials display symmetrical stress contours about the crack tip. It is interesting to note that, prior to the application of applied load, when stress is due solely to thermal residual stress, stress distribution was concentrated ~20 μm in front of the crack tip, whereas the application of a load resulted in a concentration of stress at the crack tip. This phenomenon is believed to result from localized plastic yielding when the crack arrived caused by its crack-tip stress singularity. After the crack tip was mechanically unloaded, this yielding led to a change in the local residual stress. Upon mechanically reloading the crack-tip, stresses reformed at the crack tip.

The low- and high-resolution stress maps for the 30Al composite are given in Figs. 6 and 7. The higher volume fraction of aluminium and the more complex phase morphology further increased the stress distribution within the alumina phase, as demonstrated by the larger thermal stress distribution from 97 to −391 MPa in the low-resolution map and from 84 to −349 MPa in the higher-resolution map. The smaller coefficient of thermal expansion of the alumina phase as compared to the aluminium implies that the alumina phase should be in compression, while the complex microstructure results in the observed thermal stress variation (Figs. 6a and 7a). Additionally, with the crack-tip located very close to the aluminium–alumina interface the localized crack-tip stresses could not be measured, and their influence on the localized stress distributions were not apparent. The effect of the applied load on the stress distribution is not clearly evident (Figs. 6b and 7b) but, by removing the influence of the thermal stress, the crack-tip stress field is more clearly observed. For the low-resolution crack-tip stress map, a FEM simulation for a single-phase composite with effective composite properties is superimposed on the graph, showing that the macroscopic (global) stress contours are similar.

The thermal stress distributions measured in 3Al and 30Al are within the range of that measured by others [16–18,27]. The higher stresses measured within the studies by Pezzotti and Sbaizero [27] and Hoffman et al. [17,18] are believed to result from the finer phase morphology in the composites studied, as described in Ref. [16].

4.4. Subsequent crack extension

The subsequent crack extension for the 3Al and 30Al composites are shown in Figs. 2c and 3c, respectively. For the 3Al, the crack was incrementally extended 13 times, for a total of ~520 μm of crack extension from the initial pre-crack. The Fig. 2c micrograph was taken after the last crack extension, thus, the crack opening in the vicinity of the "old" pre-crack crack-tip region is much larger, allowing for crack observation.

The subsequent crack extension for the 30Al sample was much more complex (Fig. 3c). The crack was incrementally extended eight times, for a total of ~260 μm of crack extension from the initial pre-crack. The fracture path is tortuous, discontinuous and kinked, and occurs preferentially in the alumina phase. The sequence of the subsequent crack extension is labeled *i–v*. The first observed crack extension, *i*, occurred from the crack tip; however, it is not clear whether this was a new crack extension or further crack opening, which then allowed the crack to be observed. The second crack extension, *ii*, appeared to initiate from the tip of the metal inclusion, within the alumina region of interest, and the crack gradually extended from right to left, toward the pre-existing crack. The third crack extension initiated in the middle of the alumina, at the location marked, *iii*, and the crack grew slowly in both directions. As this crack grew, so did crack *ii*. The fourth crack extension, *iv*, was a fast "pop-in" crack. During loading for this crack extension, both the *ii* and *iii* cracks grew slowly in length and the crack opened. During the fifth crack extension, v_a and v_b, cracks formed simultaneously and grew slowly. Interestingly, it appears that the crack extension *iv* was farther ahead of the crack-tip region than v_a, which further demonstrates the complex nature of fracture within these materials.

5. Discussion

The fracture behaviour of the Al–Al_2O_3 composite system was dominated by the preferential fracture of the alumina phase. Since the near-crack-tip stress fields dictate the localized fracture behaviour, insight as to the location of the subsequent crack extension can be obtained by measuring the stress distribution within the alumina. The fluorescence spectroscopy technique used in the current study was able to measure the crack-tip stress distribution within the alumina phase resulting from an applied load and from thermal residual stress. By adjusting the resolution of the measurement technique, feature sizes of ~20 μm could be resolved.

5.1. Crack-tip stress distribution

The two composites investigated in the current study had significantly different microstructures, and thus different crack-tip stress evolution. For the 3Al composite, the crack tip was located within an alumina region, allowing for stress measurements at the crack tip and in its immediate surroundings. The comparison between the measured and the FEM-simulated hydrostatic stress contours showed a clear correlation, in which the magnitudes and the general contour shapes were similar. In particular, both the measured and FEM stress contours showed asymmetrical crack-tip stress contours and compressive stress regions on the left and right sides of the large aluminium inclusion (labeled "Al" in Fig. 4a and b). Once the thermal stress was removed, the stress contours resulting from the applied load did not show the compressive stress next to the inclusion, suggesting that the method of removing the thermal stress from the fluorescence measurements was effective and afforded assessment of the stress distribution resulting solely from the applied load.

The stress magnitude that was measured in the immediate vicinity of the crack tip was nearly the same for both the low- and high-resolution measurements, showing good consistency in the measurement technique. However, the measured crack-tip stresses were lower than those predicted by the FEM simulations and showed a smaller reduction in stress with increasing distance from the crack tip. This difference between the fluorescence measurements and the FEM simulations may result from the spatial resolution of the fluorescence spectroscopy technique, in which the measured stress would be an average of the signal coming from each measurement interaction volume. For the higher-resolution measurements, the laser spot size was 5 μm; however, due to the translucency of the alumina, the interaction volume may be tens of microns in size. Additionally, it is also possible that surface displacements perpendicular to the surface plane in the immediate vicinity of the crack tip, which were similar to those observed in the AFM study of Kinoshita [8], may have affected the surface stress.

For the 30Al composite, the complex microstructure resulted in a large stress distribution within the alumina phase. From Fig. 6c it appears that the long-range crack-tip stress fields, where distances from the crack tip are greater than the scale of the microstructure, were nearly symmetrical about the crack-tip region, suggesting that generally crack propagation will continue straight through the composite. Only the higher-resolution stress measurement technique could be used to resolve the localized crack-tip stress distributions. The localized microstructure surrounding the crack tip was asymmetrical and resulted in asymmetrical crack-tip stress fields from residual stress (Fig. 7a) and from the applied load (Fig. 7c). By considering the total stress distribution (Fig. 7b), the driving force for the observed crack kinking (Fig. 3c) can be revealed. The significance of this observation is that, although the influences of the residual microstress on the crack-tip stress fields have been considered by other studies theoretically, they have not been shown experimentally to modify the fracture behaviour at a microstructural scale, as has been revealed here.

5.2. Crack extension direction

For the 3Al composite, the measured and FEM-simulated stress distributions were used to predict the subsequent crack extension direction of the initial crack. The stress distribution maps demonstrated considerable stress concentration at the crack tip, which was larger than at any other feature within the composite (Figs. 4 and 5). Hence, continued crack propagation from the pre-existing crack is to be expected. However, from the anisotropy in the measured hydrostatic stress maps it is difficult to estimate the crack deflection angle. From the FEM-simulated stress distribution the subsequent crack extension direction from the pre-existing crack could be estimated using the maximum tangential stress (MTS) criterion [42,43]. The resulting crack deflection occurs where the hoop stress at the crack tip is maximized

$$\tan\left(\frac{\theta}{2}\right) = \frac{2 - 2\sqrt{1 + 8\tan\Psi}}{8\tan\Psi} \tag{4}$$

$$\Psi = \tan^{-1}\left(\frac{k_{\mathrm{II}}}{k_{\mathrm{I}}}\right) \tag{5}$$

Here, θ is the crack deflection angle and Ψ is the crack-tip mode-mixity, which is determined from the crack-tip stress intensity factors. The FEM-predicted crack deflections were ~3.5° for the total stress distribution and ~1.5° for the applied load stress distribution, and these are schematically shown in Fig. 5b and c. The predicted crack deflection demonstrates that the presence of the aluminium phase caused a small loading asymmetry at the crack tip. The difference in the predicted deflection angles for the total and the applied load stress distributions demonstrates that the residual stress within the composite can also influence crack deflection. This is consistent with other studies investigating the influence of macroscopic residual stress on the resulting macroscopic crack deflection within graded composites [44].

The FEM-predicted crack deflection angles are similar to the observed crack extension (Fig. 2c). From the pre-existing crack tip the amount of crack deflection was estimated to be ~8° (based on the initial ~50 μm of crack extension). The difference between the measured and the predicted crack deflection angles may have resulted from assuming a 2D microstructure in FEM simulations vs. the actual 3D nature of the composite material.

For the 30Al composite, prediction of the subsequent crack extension is more difficult, as the crack-tip regularly terminated at the aluminium–alumina interface and there was minimal stress concentration within the alumina surrounding the crack tip. It was apparent, however, that continued crack extension from the pre-existing crack tip into the ductile aluminium phase was unlikely to occur. By comparing the measured total stress distributions in Fig. 7b to the final crack extension (Fig. 3c), it can be seen that the crack reinitiated from within the same alumina region as the crack tip in a region where there was a tensile hydrostatic stress (cracks *ii* and *iii*). For further crack extension, crack *iv*, this crack appears to have extended in a region of compressive stress. However, as the crack extends the stress distribution within the composite will change, thus the actual stress distribution in the region of crack *iv* had changed after the formation of cracks *ii* and *iii*.

This analysis shows that fluorescence spectroscopy can be effectively used for measuring the stress distribution within complex microstructure composites and can highlight the localized stress concentrations within the composite microstructure that may increase the likelihood of crack initiation and crack propagation.

6. Conclusions

Fluorescence microprobe spectroscopy was used to directly measure the stress distributions that develop within interpenetrating Al–Al_2O_3 composites, and these were compared to FEM simulations and in situ crack propagation experiments. The following conclusions can be drawn from this work.

(1) The fluorescence spectroscopy technique was able to measure the macroscopic and microscopic stress distributions that develop within the neighbourhood of the crack-tip region of complex composite microstructures, where the stress distribution around inclusions of ~20 μm in diameter could be resolved. This high spatial resolution made it possible to investigate how the crack-tip stress distribution changed as a result of the microstructure, thermal residual stress and applied stress.
(2) For the 3Al composite, the stress concentration at the crack-tip resulting from the applied load was observed. The stress magnitude and stress contour shape were similar for the low- and high-resolution measurements, demonstrating consistency in the measurement technique.
(3) The FEM simulation for the 3Al composite generally provided stress magnitudes and contour shapes that were similar to the fluorescence-measured stress. However, the stress in the immediate vicinity of the crack tip was much lower for the fluorescence-measured stress than for the FEM simulations. This difference was believed to result from the averaging of the measured stress within the measurement interaction volume.
(4) For the 30Al composite, the long-range crack-tip stress fields appeared to be nearly symmetrical about the crack-tip, leading to a general "straight" macroscopic fracture path through the composite. In contrast, the localized microstructure asymmetry in the immediate vicinity of the crack-tip resulted in short-range crack-tip stress asymmetry. Both of these factors contributed to the microscopic crack kinking observed in the composite.

Acknowledgements

The authors sincerely thank Dr. Achim Neubrand and Emil Aulbach of the Technische Universität Darmstadt, Germany for assistance during sample preparation. Additionally, the authors thank Dr. Mathew Tilbrook and Dr. Lyndal Rutgers of the University of New South Wales, for useful discussions on using ANSYS and providing the epoxy–alumina sample, respectively. This work was supported by the Australian Research Council, the Australian Academy of Science and the Japan Society for the Promotion of Science.

References

[1] Kassam ZHA, Zhang RJ, Wang Z. Mat Sci Eng 1995;A203:286.
[2] Gu P, Asaro RJ. Int J Solid Struct 1997;34(24):3085.
[3] Wang C, Libardi W, Baldo JB. Int J Fract 1998;94:177.
[4] Masud A, Zhang Z, Botsis J. Composits Part B 1998;29B:577.
[5] Li Z, Chen Q . Eng Fract Mech 2003;70:581.
[6] Kim AS, Suresh S. Int J Solid Struct 1997;34(26):3415.
[7] Bennett JA, Young RJ. Comp Sci Technol 1997;57:945.
[8] Kinoshita T. Acta Mater 1998;46(11):3963.
[9] Butcher RJ, Rousseau CE, Tippur HV. Acta Mater 1999;47(1):259.
[10] Kawagishi Y, Shozu M, Hirose Y. Mech Mater 2001;33:741.
[11] Miyagawa H, Sato C, Ikegami K. Composites Part A 2001;A32:477.
[12] Miyagawa H, Sato C, Ikegami K. Mech Mater 2002;34:179.
[13] Hanan JC, Ustundag E, Beyerlein IJ, Swift GA, Almer JD, Lienert U, et al. Acta Mater 2003;51:4239.
[14] Preuss M, Rauchs G, Doel T, Steuwer A, Bowen P, Withers P. Acta Mater 2003;51:1045.
[15] Diaz FA, Yates JR, Patterson EA. Int J Fatigue 2004;26:365.
[16] Moon RJ, Hoffman M, Tochino S, Lee CJ, Pezzotti G. J Mater Sci 2006;41:7571.
[17] Hoffman M, Skirl S, Pompe W, Rödel J. Acta Mater 1999;47(2):565.
[18] Hoffman M, Rödel J, Skirl S, Zimmermann A, Fuller E, Müllejans H. Key Eng Mater 1999;159–160:311.
[19] Belnap JD, Shetty DK. Comp Sci Techol 1998;58:1763.
[20] Pezzotti G, Müller WH. Continuum Mech Thermodyn 2002;14:113.
[21] Ma Q, Clarke DR. J Am Ceram Soc 1993;76:1433.
[22] He J, Clarke DR. J Am Ceram Soc 1995;78:1347.
[23] He J, Beyerlein IJ, Clarke DR. J Mech Phys Solids 1999;47:465.
[24] Yu H, Clarke DR. J Am Ceram Soc 2002;85(8):1966.
[25] Agrawal P, Sun CT. Comp Sci Technol 2004;64:1167.
[26] Agrawal P, Conlon K, Bowman KJ, Sun CT, Cichocki FR, Trumble KP. Acta Mater 2003;51:1143.
[27] Pezzotti G, Sbaizero O. Mat Sci Eng 2001;A303:267.
[28] Prielipp H, Knechtel M, Claussen N, Streiffer S, Müllejans H, Rühle M, et al. Mater Sci Eng 1995;A197:19.
[29] Stech M, Rödel J. J Am Ceram Soc 1996;79(2):291.
[30] Nagendra N, Jayaram V. J Mater Res 2000;15(5):1131.
[31] Raddatz O, Schneider GA, Claussen N. Acta Mater 1998;46(18):6381.
[32] Neubrand A, Chung T-J, Rödel J, Steffler ED, Fett T. J Mater Res 2002;17(11):2912.
[33] Cichocki Jr FR, Trumble KP, Rödel J. J Am Ceram Soc 1998;81(6):1661.
[34] Kübler J. Ceram Eng Sci Proc 1997;18:155.
[35] Flinn BD, Lo CS, Zok FW, Evans AG. J Am Ceram Soc 1993;76(2):369.
[36] Tilbrook MT, Moon RJ, Hoffman M. Mater Sci Eng 2005;A393:170.
[37] Moon RJ, Hoffman M, Bowman KJ, Trumble KP. Acta Mater 2001;49(6):995.
[38] Moon RJ, Bowman KJ, Trumble K, Rödel J. J Am Ceram Soc 2000;83(2):445.
[39] Kocks UF. J Eng Mater Technol 1976;98(1):76.
[40] Moon RJ, Hoffman M, Hilden J, Bowman KJ, Trumble K, Rödel J. Eng Fract Mech 2002;69:1647.
[41] Moon RJ, Hoffman M, Hilden J, Bowman KJ, Trumble K, Rödel J. J Am Ceram Soc 2002;85(6):1505.
[42] Erdogan F, Sih GC. J Basic Eng ASME Trans 1963;85:519.
[43] Tilbrook MT, Moon RJ, Hoffman M. J Comp Sci Techol 2005;65(2):201.
[44] Chapa-Cabrera J, Reimanis I. Eng Fract Mech 2002;69:1667.
[45] McLellan RB, Ishikawa T. J Phys Chem Solids 1987;48:603.
[46] Shen YL, Suresh S. Acta Mater 1996;44(4):1337.
[47] Touloukian YS. Thermophysical properties of matter: thermal expansion of metallic elements and alloys, vol. 12. New York: Plenum Publishing; 1977. p. 2.
[48] Skirl S, Hoffman M, Bowman K, Wiederhorn S, Rödel J. Acta Mater 1998;46(7):2493.
[49] Soga N, Anderson OL. J Am Ceram Soc 1966;49(7):355.
[50] Kingery WD, Bowen HK, Uhlmann DR. Introduction to ceramics. second ed. Brisbane: John Wiley & Sons; 1976.
[51] Hillman C, Suo Z, Lange F. J Am Ceram Soc 1996;79(8):2127.
[52] Moon RJ, Tilbrook MT, Neubrand A, Hoffman M. J Am Ceram Soc 2005;88(3):666.